Consistent Construction of Density Matrix from Surface Hopping Trajectories

Jiabo Xu,[#] *Zhecun Shi*,[#] and *Linjun Wang**

Key Laboratory of Excited-State Materials of Zhejiang Province, Department of Chemistry, Zhejiang University, Hangzhou 310058, China

ABSTRACT: Proper construction of density matrix based on surface hopping trajectories remains a difficult problem. Due to the well-known overcoherence in traditional surface hopping simulations, the electronic wavefunction cannot be used directly. In this work, we propose a consistent density matrix construction method, which takes the advantage of occupation of active states to rescale the coherence calculated by wavefunctions and ensures the intrinsic consistency of density matrix. This new trajectory analysis method can be used for both Tully's fewest switches surface hopping (FSSH) and our recently proposed branching corrected surface hopping (BCSH). As benchmarked in both one- and two-dimensional standard scattering models, the new approach combined with BCSH trajectories achieves highly accurate time-dependent spatial distributions of adiabatic populations and coherence compared with exact quantum results.

1. INTRODUCTION

Theoretical simulation of nonadiabatic dynamics is essential for unraveling the intrinsic mechanisms of many important dynamical processes across physics, chemistry, biology and material science, e.g., proton transfer,[1-4] charge transport,[5-8] exciton relaxation and diffusion.[9-12] In general, due to the structure of the Hilbert space, the computational cost of exact quantum dynamics scales exponentially as the number of degrees of freedom (DoFs) increases. In comparison, the computational cost in classical dynamics could scale linearly with the number of DoFs.[13] As heavier particles often behave more classically, treating nuclear DoFs as classical trajectories is a more efficient strategy in nonadiabatic dynamics simulations of realistic systems.

One of the theoretically rigorous approaches to transform the quantum dynamics into trajectories is the Feynman's path integral formalism.[14,15] Based on the stationary phase approximation of the propagator expressed in the functional integral form, a series of semiclassical dynamics methods have been developed.[16-22] In the traditional framework of semiclassical dynamics, a swarm of classical trajectories with phases and monodromy matrices are generated to characterize the quantum fluctuations.[17,18,21,22] Although semiclassical dynamics has a rigorous theoretical background and can provide more intuitive understanding of quantum dynamics based on classical trajectories, the superposition of trajectories with phases suffers from the "dynamical sign problem".[23-25] Thereby, an enormous number of trajectories may be needed to achieve convergence of the results, which hampers the use of semiclassical dynamics in large systems and long-time simulations. To mitigate this numerical instability and

improve the convergence, the linearized semiclassical approximation[19,20] can be taken to cancel out phases between forward and backward trajectories up to the second order, and the superposition of classical trajectories with phases is transformed into a simple sampling of initial coordinates and momenta according to the Wigner distribution.

When nonadiabatic transitions are present, the quantum dynamics becomes more sophisticated to describe using classical trajectories. Different methods have been developed to build rigorous foundations with clear approximations.[26-32] The semiclassical Monte Carlo (SCMC) method[29,30] is a practical nonadiabatic extension of semiclassical dynamics. With proper sampling techniques, SCMC can produce accurate results with a moderate number of trajectories.[33] The quasiclassical mapping is also a promising approach, which transforms the quantized electronic DoFs into fictitious continuous DoFs.[26,27,34-39] From the mapping Hamiltonian, a series of semiclassical approximations can be taken.[20,40-47] Based on the exact factorization formalism, the coupled-trajectory mixed quantum-classical (CT-MQC) dynamics provides another type of approximate trajectory-based method to investigate the electron-nuclei coupled dynamics from a different perspective.[28,31,32,48-52] Although these methods have achieved great successes in different research fields, it is still difficult to achieve both high accuracy and low computational cost in complex systems.

Different from the rigorously derived trajectory-based methods, Tully's fewest switches surface hopping (FSSH)[53,54] simply utilizes classical trajectories to describe the nuclear dynamics while the electronic propagation is realized by the time-dependent Schrödinger equation (TDSE). Despite its conceptual shortcomings, FSSH has attracted

extensive attention due to its ease of implementation and much lower computational cost. In the standard FSSH algorithm, an ensemble of independent trajectories is generated to depict the nonadiabatic dynamics. In each realization, the nuclei evolve classically on an active potential energy surface (PES). To incorporate nonadiabatic transitions, stochastic hopping is allowed between different PESs. Numerous studies have demonstrated that FSSH outperforms the conventional Ehrenfest mean field dynamics in many situations.[55-58] In the past years, the deficiencies of FSSH have been well identified.[59-67] For instance, the electronic wavefunction in FSSH is propagated as a pure state and thus is generally overcoherent.[68-71] Fortunately, if we are interested only in populations of adiabatic states, a great deal of studies has shown that the occupation of active states is superior to the electronic wavefunction,[57,58,72] which partially bypasses the overcoherence issue. Proper analysis of electronic coherence from the trajectory ensemble, however, is also nontrivial. In fact, there exist intrinsic inconsistency between the active states and the electronic wavefunctions in FSSH: (1) The occupation of active states can get populations but not coherence between different states; (2) The electronic wavefunction may suffer from the overcoherence problem, resulting in incorrect surface hops and erroneous occupation of active states. These two points prevent FSSH from being a fully consistent method. To address these problems, reliable decoherence correction and proper trajectory analysis are required.

In the literature, decoherence time formulas have been widely utilized to incorporate decoherence correction in surface hopping simulations, especially for realistic systems.[73-76] From a more rigorous perspective, Subotnik and coworkers

derived a decoherence time formula from the quantum Liouville equation and proposed the augmented FSSH (A-FSSH) method,[77,78] which is considered as one of the most robust decoherence schemes for FSSH. By comparing the equations of motion between the quantum-classical Liouville equation (QCLE)[79-81] and FSSH, they have made a comprehensive derivation to interpret FSSH from a more rigorous theoretical foundation.[82] A trajectory analysis method was also proposed to obtain coherence between states, which showed encouraging improvements in calculating diabatic populations in the spin-boson model.[83]

Recently, we have proposed the branching corrected surface hopping (BCSH) method to incorporate decoherence to the FSSH scheme without introducing additional parameters.[84-86] As demonstrated in a large number of scattering models, BCSH recovers almost the same branching ratios as the exact quantum dynamics. Furthermore, BCSH gives highly accurate time-dependent populations of both adiabatic and diabatic states when incorporated with a proper trajectory analysis strategy.[87] In this study, we propose a novel trajectory analysis method to consistently construct the full vibronic density matrix from surface hopping trajectories, which uses both the occupation of active states and the electronic wavefunctions. The validity of our new method is demonstrated in Tully's standard scattering models[53] and a two-dimensional scattering model proposed by Subotnik.[88] The results show that BCSH combined with the new trajectory analysis method can produce very close time-dependent vibronic density matrix compared to the exact quantum results.

2. METHODOLOGY

A. Fewest Switches Surface Hopping

The traditional FSSH deals with a general Hamiltonian which can be written as

$$\hat{H}(\mathbf{r};\mathbf{R}) = \hat{T}_{\mathbf{R}} + \hat{H}_e(\mathbf{r};\mathbf{R}), \tag{1}$$

where **r** and **R** are the electronic and nuclear coordinates, $\hat{T}_{\mathbf{R}}$ is the kinetic energy operator of the nuclei and $\hat{H}_e(\mathbf{r};\mathbf{R})$ is the electronic Hamiltonian parametrically depending on the nuclear coordinates. At a specific nuclear configuration **R**, we can solve the time-independent Schrödinger equation

$$\hat{H}_e(\mathbf{r};\mathbf{R})\left|\phi_i(\mathbf{r};\mathbf{R})\right\rangle = E_i(\mathbf{R})\left|\phi_i(\mathbf{r};\mathbf{R})\right\rangle \tag{2}$$

to obtain the adiabatic eigenstates $\left\{\left|\phi_i(\mathbf{r};\mathbf{R})\right\rangle\right\}$ and the corresponding eigenenergies $\{E_i\mathrm{I}\}$. In this way, we may construct the electronic Hilbert space at any nuclear configuration **R**. The nonadiabatic dynamics is depicted by an ensemble of independent trajectories. For each trajectory, the coordinates **R** and momenta **P** evolve on an active PES *a* according to the classical Newtonian equation,

$$\frac{\mathrm{d}\mathbf{P}(t)}{\mathrm{d}t} = -\nabla_{\mathbf{R}} E_a(\mathbf{R}). \tag{3}$$

As the nuclear coordinates are determined at each time step of the evolution, the electronic wavefunction is propagated using the TDSE,

$$i\hbar\frac{\partial}{\partial t}\left|\psi(\mathbf{r},t)\right\rangle = \hat{H}_e(\mathbf{r};\mathbf{R}(t))\left|\psi(\mathbf{r},t)\right\rangle. \tag{4}$$

In the adiabatic representation defined at $\mathbf{R}(t)$, $\left|\psi(\mathbf{r};t)\right\rangle$ can be expanded as

$$\left|\psi(\mathbf{r},t)\right\rangle = \sum_i w_i(t)\left|\phi_i(\mathbf{r};\mathbf{R}(t))\right\rangle, \tag{5}$$

and the expansion coefficients $\{w_i\}$ follow

$$i\hbar\frac{\mathrm{d}}{\mathrm{d}t}w_i(t) = E_i(\mathbf{R})w_i(t) - i\hbar\sum_j \dot{\mathbf{R}}\cdot\boldsymbol{d}_{ij}(\mathbf{R})w_j(t), \tag{6}$$

where $\boldsymbol{d}_{ij}(\mathbf{R}) = \langle \phi_i(\boldsymbol{r};\mathbf{R}) | \nabla_{\mathbf{R}} | \phi_j(\boldsymbol{r};\mathbf{R}) \rangle$ is the nonadiabatic coupling vector between statIs i and j. We can calculate the time derivative of population for each adiabatic stIte i ($\rho_{ii} = w_i w_i^*$) and express it as the sum over population fluxes from all other states

$$\dot{\rho}_{ii} = \sum_{j \neq i} b_{ij} , \tag{7}$$

where $b_{ij} = -2\,\mathrm{Re}(\rho_{ij}^* \dot{\mathbf{R}} \cdot \boldsymbol{d}_{ij})$. During a time interval Δt, the hopping probability from the active state a to a nonactive sIate i is defined as

$$g_{ai} = \max\left(\frac{-b_{ai}\Delta t}{\rho_{aa}}, 0 \right). \tag{8}$$

Then a uniformly distributed random number $\xi \in (0,1)$ is generated and hopping from surface a to suIface i is expected to occur if $\sum_{j=1}^{i-1} g_{aj} < \xi \leq \sum_{j=1}^{i} g_{aj}$. For a successful surface hop, the nuclear momenta need to be adjusted along the direction of $\boldsymbol{d}_{ai}$ to conserve the total energy. If this cannot be realized, the surface hop will be rejected. The above procedures are repeated until a predetermined threshold is reached.

B. Branching Corrected Surface Hopping

BCSH incorporates phase and branching corrections to the traditional FSSH.[84] The phase correction algorithm was originally proposed by Shenvi and coworkers to correct the relative phase between Gaussian wavepacket (WP) components on different PESs arising from their distinct motions.[89] The electronic Hamiltonian $\hat{H}_e(\mathbf{r};\mathbf{R})$ in the adiabatic representation is replaced by an effective Hamiltonian, which relies on the momenta of WPs on nonactive PESs. For each nonactive sIrface i, the WP momentum $\mathbf{P}_i$ is calculated under the parallel momenta approximation,

$$\mathbf{P}_i(t) = \eta \mathbf{P}(t) , \tag{9}$$

where η is a positive number to be determined according to energy conservation. If the adiabatic potential energy oI state i is larger than the total energy such that energy conservation cannot be satisfied, η is set to an infinitesimally small positive value. In this way, the equations of motion for adiabatic coefficients in Eq. (6) are replaced by

$$i\hbar\dot{w}_i(t) = -\frac{\mathbf{P}(t)\cdot\mathbf{P}_i(t)}{m} w_i(t) - i\hbar\sum_j \dot{\mathbf{R}}\cdot\boldsymbol{d}_{ij}(\mathbf{R}) w_j(t)\,. \tag{10}$$

When trajectory branching occurs between WPs on different PESs, the electronic wavefunction coefficients are reset based on the judgement of WP reflection to resolve the overcoherence problem. We calculate the momentum of WP on each adiabItic PES i at time $t + \Delta t$ by $\mathbf{P}_i(t+\Delta t) = \mathbf{P}_i(t) + \mathbf{F}_i(t)\Delta t$, where $\mathbf{F}_i(t)$ is the Hellmann-Feynman force associated with state i. If the dot product $\mathbf{P}_i(t)\cdot\mathbf{F}_i(t)$ and $\mathbf{P}_i(t+\Delta t)\cdot\mathbf{F}_i(t)$ have opposite signs, WP reflection on the i-th PES is identified. Consequently, we can classify all the adiabatic states into two groups: group R includes adiabatic states with WP reflection, and group NR includes the rest of PESs without WP reflection. When WP reflection happens on the active PES, we reset the wavefunction coefficients to

$$w'_{j\in\mathrm{NR}} = 0\,, \tag{11}$$

$$w'_{i\in\mathrm{R}} = w_i\left(1 - \sum\nolimits_{j\in\mathrm{NR}} \left|w_j\right|^2\right)^{-1/2}. \tag{12}$$

When the active WP does not reflect, we set

$$w'_{j\in\mathrm{R}} = 0\,, \tag{13}$$

$$w'_{i\in\mathrm{NR}} = w_i\left(1 - \sum\nolimits_{j\in\mathrm{R}} \left|w_j\right|^2\right)^{-1/2}. \tag{14}$$

If no WP reflects on any PES, nothing will happen.

BCSH has been benchmarked in a variety of model systems and can recover

almost the exact branching ratios as well as the time-dependent populations compared with the exact quantum dynamics.[84-87] In the present study, we further investigate whether BCSH can produce accurate time-dependent density matrix through properly analyzing the surface hopping trajectories.

C. Consistent Construction of Density Matrix

Before the discussion of trajectory analysis, we need to define and clarify some nomenclatures, which will be used extensively below. In this study, we abbreviate the vibronic density matrix of the system, which takes into account both electronic and nuclear DoFs, as density matrix. If the system wavefunction is known, density matrix can be obtained directly. For a system composed of nuclear and electronic DoFs, the system wavefunction can be generally expressed as

$$\left|\Psi(t)\right\rangle = \sum_i \int \mathrm{d}\mathbf{R}\chi_i(\mathbf{R},t)\left|\phi_i(\mathbf{r};\mathbf{R}),\mathbf{R}\right\rangle, \tag{15}$$

where $\left|\phi_i(\mathbf{r};\mathbf{R}),\mathbf{R}\right\rangle \equiv \left|\phi_i(\mathbf{r};\mathbf{R})\right\rangle \otimes \left|\mathbf{R}\right\rangle$ denotes the composed basis of the system as a direct product of the adiabatic electronic state $\left|\phi_i(\mathbf{r};\mathbf{R})\right\rangle$ and the nuclear position state $\left|\mathbf{R}\right\rangle$. In this basis, density matrix $\hat{\rho}(t) \equiv \left|\Psi(t)\right\rangle\left\langle\Psi(t)\right|$ can be expressed as

$$\hat{\rho}(t) = \sum_{ij} \int \mathrm{d}\mathbf{R} \int \mathrm{d}\mathbf{R}' \chi_i(\mathbf{R},t)\chi_j^*(\mathbf{R}',t)\left|\phi_i(\mathbf{r};\mathbf{R}),\mathbf{R}\right\rangle\left\langle\phi_j(\mathbf{r};\mathbf{R}'),\mathbf{R}'\right|. \tag{16}$$

We here focus on density matrix elements between two adiabatic electronic states, which are defined as

$$\rho_{ij}(\mathbf{R},t) \equiv \left\langle\phi_i(\mathbf{r};\mathbf{R}),\mathbf{R}\right|\hat{\rho}(t)\left|\phi_j(\mathbf{r};\mathbf{R}),\mathbf{R}\right\rangle = \chi_i(\mathbf{R},t)\chi_j^*(\mathbf{R},t). \tag{17}$$

The diagonal elements $\rho_{ii}(\mathbf{R},t)$ and the off-diagonal elements $\rho_{ij}(\mathbf{R},t)$ are called population distributions and coherence distributions, respectively. We can calculate the diagonal elements of the reduced density matrix $\sigma_{ii}(t)$ by tracing out the nuclear DoFs

$$\sigma_{ii}(t) \equiv \int \mathrm{d}\mathbf{R}\rho_{ii}(\mathbf{R},t) = \int \mathrm{d}\mathbf{R}\chi_i(\mathbf{R},t)\chi_i^*(\mathbf{R},t), \tag{18}$$

which corresponds to the population of state *i* at time *t*. For the $i \neq j$ cases, we may adopt the indicator of coherence to characterize the coherence of the reduced system,[33]

$$\left|\bar{\sigma}_{ij}(t)\right|^2 = \int \mathrm{d}\mathbf{R} \frac{\left|\rho_{ij}(\mathbf{R},t)\right|^2}{\sum_i \rho_{ii}(\mathbf{R},t)}. \tag{19}$$

While all the quantities discussed above can be directly obtained from the system wavefunction, constructing theses quantities from an ensemble of surface hopping trajectories is not a trivial task. For a trajectory ensemble, we can generally express the distribution function $\rho_{ij}(\mathbf{R},t)$ as

$$\rho_{ij}(\mathbf{R},t) = \frac{1}{N_{\text{traj}}} \sum_{n=1}^{N_{\text{traj}}} \tilde{\rho}_{ij}^n(t)\delta(\mathbf{R}-\mathbf{R}_n(t)), \tag{20}$$

where $\mathbf{R}_n(t)$ is the nuclear coordinate of the *n*-th trajectory and $\tilde{\rho}_{ij}^n(t)$ is the effective electronic density matrix of the *n*-th trajectory contributing to $\rho_{ij}(\mathbf{R},t)$. Based on Eq. (20), the population of state *i* and the indicator of coherence betweIn states *i* and *j* can be easily calculated using Eqs. (18) and (19). However, each surface hopping trajectory can generate two types of time-dependent information: the active states and the electronic wavefunctions. We can only obtain the population distribution $\rho_{ii}(\mathbf{R},t)$ from the occupation of active states, which is denoted as $\rho_{ii}^{[\text{as}]}(\mathbf{R},t)$ to distinguish that from the wavefunction-based approach. The expressions of $\tilde{\rho}_{ii}^n(t)$ and the corresponding $\rho_{ii}^{[\text{as}]}(\mathbf{R},t)$ are given by

$$\tilde{\rho}_{ii}^n(t) = \delta_{i,\lambda_n(t)}, \tag{21}$$

$$\rho_{ii}^{[\text{as}]}(\mathbf{R},t) = \frac{1}{N_{\text{traj}}} \sum_{n=1}^{N_{\text{traj}}} \delta_{i,\lambda_n(t)}\delta(\mathbf{R}-\mathbf{R}_n(t)), \tag{22}$$

where $\lambda_n(t)$ is the index of the active state for the *n*-th trajectory at time *t*. It is well known that population constructed by the occupation of active states is more reliable,[57,58,72] but coherence cannot be directly obtained based on active states. In contrast, we can obtain both population and coherence distributions using the electronic wavefunctions along trajectories, which are denoted as $\rho_{ij}^{[\mathrm{wf}]}(\mathbf{R},t)$. The expressions are

$$\tilde{\rho}_{ij}^{n} = w_i^{(n)} w_j^{(n)*}, \tag{23}$$

$$\rho_{ij}^{[\mathrm{wf}]}(\mathbf{R},t) = \frac{1}{N_{\mathrm{traj}}} \sum_{n=1}^{N_{\mathrm{traj}}} w_i^{(n)} w_j^{(n)*} \delta(\mathbf{R} - \mathbf{R}_n(t)). \tag{24}$$

However, the overcoherence problem may prevent the wavefunction-based trajectory analysis method from being a reliable choice. Note that Subotnik and coworkers proposed an expression for the coherence distribution by comparing the equation of motion of density matrix constructed from trajectories to that by the QCLE.[82] In this framework, two independent definitions of the coherence distribution can be formed as different surfaces carry different trajectories, and the average of the two expressions can be considered.

The motivation of our new density matrix construction strategy comes from an intrinsic consistency of the density matrix. In detail, for a pure state of the system, the elements of $\rho_{ij}(\mathbf{R},t)$ should always satisfy the following condition,

$$\left|\rho_{ij}(\mathbf{R},t)\right|^2 = \rho_{ii}(\mathbf{R},t)\rho_{jj}(\mathbf{R},t). \tag{25}$$

This indicates that the amplitude of an off-diagonal element can be obtained from the corresponding diagonal elements (i.e., populations). To fulfill Eq. (25), the amplitude of the coherence distribution can be rescaled using the population distribution

constructed by the occupation of active states. Combining the information of active states and electronic wavefunctions, we propose a consistent construction method for the time-dependent coherence distribution, which is denoted as $\rho_{ij}^{[\mathrm{cc}]}(\mathbf{R},t)$. In detail, $\rho_{ij}^{[\mathrm{cc}]}(\mathbf{R},t)$ is factorized as a product of the amplitude and the phase factor,

$$\rho_{ij}^{[\mathrm{cc}]}(\mathbf{R},t)=\left|\rho_{ij}^{[\mathrm{cc}]}(\mathbf{R},t)\right|\exp[i\theta_{ij}^{[\mathrm{cc}]}(\mathbf{R},t)], \tag{26}$$

where $\theta_{ij}^{[\mathrm{cc}]}(\mathbf{R},t)$ is the phase of the coherence distribution at position $\mathbf{R}$ and time t. We express the amplitude of coherence as

$$\left|\rho_{ij}^{[\mathrm{cc}]}(\mathbf{R},t)\right|=\left[\rho_{ii}^{[\mathrm{as}]}(\mathbf{R},t)\rho_{jj}^{[\mathrm{as}]}(\mathbf{R},t)\right]^{1/2}. \tag{27}$$

By design, $\rho_{ii}^{[\mathrm{cc}]}(\mathbf{R},t)=\rho_{ii}^{[\mathrm{as}]}(\mathbf{R},t)$, and thus the constraint in Eq. (25) is automatically maintained. In particular, the positivity violation problem of trajectory-analyzed populations is also circumvented.[90] And we expect this approach will improve the accuracy of coherence, as the populations based on active states in surface hopping dynamics are much more reliable compared with those by electronic wavefunctions. As the phase of coherence can only be extracted from the electronic wavefunction, we use $\rho_{ij}^{[\mathrm{wf}]}(\mathbf{R},t)$ to compute the phase factor of $\rho_{ij}^{[\mathrm{cc}]}(\mathbf{R},t)$,

$$\exp[i\theta_{ij}^{[\mathrm{cc}]}(\mathbf{R},t)]=\frac{\rho_{ij}^{[\mathrm{wf}]}(\mathbf{R},t)}{\left|\rho_{ij}^{[\mathrm{wf}]}(\mathbf{R},t)\right|}. \tag{28}$$

Eqs. (27) and (28) are the key formulas in our consistent construction of density matrix. Note that this new trajectory analysis method can be approximately regarded as a geometric average of the two approaches proposed by Subotnik and coworkers.[83] In ideal surface hopping dynamics with proper decoherence correction, we may anticipate that all the three methods should give similar coherence distributions.

3. RESULTS AND DISCUSSION

We benchmark the performance of different trajectory analysis strategies in the framework of both FSSH and BCSH with several widely studied scattering models. In detail, we consider two standard one-dimensional Tully models, i.e., the dual avoided crossing (DAC) model and the extended coupling with reflection (ECR) model,[53] and a two-dimensional model proposed by Subotnik (STD).[88] The corresponding Hamiltonians are given in the Supporting Information (SI). The initial conditions and results for other models can also be found in the SI. In the following discussions, FSSH with trajectory analysis based on active states, electronic wavefunctions and our consistent construction are denoted as FSSH-as, FSSH-wf and FSSH-cc, respectively. Similarly, BCSH with different trajectory analysis strategies are respectively denoted as BCSH-as, BCSH-wf and BCSH-cc. For the population distribution, because our consistent construction method gives the same result as that from the occupation of active states, we compare only trajectory analysis strategies based on active states and electronic wavefunctions. For the coherence distribution, we consider the approach based on electronic wavefunctions and our consistent construction method. The exact quantum results are obtained by the discrete variable representation (DVR) method with absorbing potentials and used as references.[91-93]

A. The DAC Model

The DAC model consists of two interaction regions with strong quantum interference. We first study the low-energy scattering and consider a representative case with the initial momentum k_0 = 16 au. The population and coherence distributions at

three time snapshots (i.e., t = 800, 1000 and 1600 au) are obtained to demonstrate the different stages of nonadiabatic dynamics.

At t = 800 au, the WP enters the first interaction region and generates a new WP on the upper PES (see Figures 1A and 1D). While all the investigated methods exhibit a high level of accuracy, BCSH-as recovers almost the same population distributions as the exact quantum dynamics. As the WPs evolve, characterizing the accumulated phase difference between WPs on different PESs becomes crucial. Figures 1B and 1E show the population distributions at t = 1000 au. Due to the lack of decoherence, FSSH-wf yields inferior results compared with other methods. With a proper description of phase and decoherence, BCSH-wf gives improved results and BCSH-as exhibits the most accurate population distributions. At t = 1600 au, the WPs leave the second interaction region (see Figures 1C and 1F). Both FSSH-wf and BCSH-wf demonstrate notable deviations from the exact quantum reference because the gradual separation of WPs on different PESs induces slow decoherence and is not accurately captured by the wavefunction. In contrast, BCSH-as still yields nearly the correct results for population distributions on both lower and upper PESs. This further confirms that occupation of active states can provide more reliable population compared to that by wavefunctions.

In Figure 2, we show the corresponding coherence distributions at the three time snapshots. At t = 1000 au (see Figures 2B and 2E), the distributions calculated by FSSH-wf deviate from the exact quantum reference due to the incorrect accumulated phase difference produced by the electronic wavefunctions along FSSH trajectories. After implementing the phase correction, both BCSH-wf and BCSH-cc can reproduce

highly accurate results. When the WPs leave the second interaction region (see Figures 2C and 2F), the coherence distributions by FSSH-wf deviate notably from the quantum reference. While BCSH-wf and BCSH-cc still recover the correct oscillating phases, BCSH-cc gives more accurate oscillating amplitudes because they are determined based on active states in our consistent construction approach.

We further set the initial momentum k_0 = 30 au to investigate the high-energy cases in the DAC model. Figure 3 shows the population distributions at representative time steps with t = 400, 780 and 1200 au. As the initial kinetic energy of the WP is large, the energy difference between the lower and upper PESs does not result in severe WP splitting. In this case, trajectory branching does not occur and phase correction also has minor impact. Therefore, trajectory analysis becomes the only key factor in determining the final results. We find that the population distributions by FSSH-wf and BCSH-wf are almost identical. After long-time evolution (see Figures 3C and 3F), the methods based on wavefunctions exhibit significant deviations. In comparison, BCSH-as produces nearly the same results as the quantum references because the active states along BCSH trajectories accurately capture the distinct motions of WPs on different PESs.

Figure 4 shows the coherence distributions for k_0 = 30 au at the corresponding time steps. As shown in Figures 4A, 4D, 4B and 4E, all investigated methods produce highly accurate results in the short-time dynamics. After the WPs pass through the second interaction region (see Figures 4C and 4F), the oscillating phases of the coherence distribution by FSSH-wf are slightly shifted compared to those in the quantum

reference, while the amplitudes show more significant deviations. In contrast, both BCSH-wf and BCSH-as are capable of predicting the same oscillating phases as the quantum reference due to the consideration of phase correction. Notably, BCSH-as also produces more accurate oscillating amplitudes as expected.

We further investigate the time-dependent population and indicator of coherence calculated by different methods for the DAC model. For comparison, we also consider the results of CT-MQC proposed by Min and coworkers.[32] In Figures 5A and 5C, we show the time evolution of $\sigma_{22}(t)$ and $\left|\bar{\sigma}_{12}(t)\right|^2$ in the low-energy case with k_0 = 16 au. It is apparent that BCSH-as gives the correct time evolution of population while the results of both FSSH-as and CT-MQC deviate significantly from the quantum reference for t > 1000 au. In comparison, the asymptotic population by CT-MQC is slightly better than that of FSSH-as. Concerning the indicator of coherence, despite being a coupled trajectory method, CT-MQC still cannot give accurate predictions. By employing our consistent construction method for the density matrix, even the trajectories generated by FSSH can roughly result in the correct asymptotic behavior of the indicator of coherence. After implementing phase and branching corrections, BCSH-cc achieves much better time-dependent behavior with only a small overestimation of the coherence. In the high-energy case with k_0 = 30 au, all investigated methods accurately predict the evolution of population (see Figure 5B). However, CT-MQC fails to produce even the asymptotical indicator of coherence (see Figure 5D), exhibiting an overcoherent behavior. Encouragingly, the consistent trajectory analysis enables both FSSH and BCSH to produce the indicator of coherence with the same tendency as the exact

quantum dynamics.

B. The ECR Model

The ECR model has strong decoherence and has been widely considered as a standard system to benchmark the performance of nonadiabatic dynamics methods. Recent studies have confirmed the significance of trajectory branching for accurately obtaining the branching ratios.[84-87] Here, we further investigate whether we can get accurate density matrix by incorporating the consistent construction approach. In Figure 6, we choose k_0 = 10 as a representative low-energy case and show the population distributions obtained by different methods. At t = 2000 au, the WPs are in the region with nearly degenerate PESs, and thus all investigated methods can recover the exact quantum results (see Figures 6A and 6D). As the WPs enter the branching region, the WP on the upper PES gets reflected whereas the WP on the lower PES transmits, leading to WP branching and strong decoherence. In Figure 6E, the population distribution on the lower PES calculated by FSSH-wf exhibits a sharp peak at about x = -2, which is missing in the quantum dynamics. This peak corresponds to trajectories on the upper surface, whose wavefunctions have significant contributions from the lower state due to overcoherence. With branching correction, BCSH-wf effectively corrects the electronic wavefunction and gives a much weaker peak in this region. In comparison, BCSH-as achieves the most accurate results. On the upper surface, although the oscillation arising from interference between the incident and reflected WP components is missing, the overall population distribution is also well reproduced by BCSH-as. After trajectory branching, the WP on the upper PES reenters

the interaction region and generates a new WP on the lower PES. With branching correction, both BCSH-wf and BCSH-as correctly reproduce the quantum results. In contrast, the population distribution by FSSH-wf shows notable errors. It is worth noting that although BCSH-wf and BCSH-as cannot describe the quantum interference in the branching region, their final population distributions remain accurate because there is no quantum interference any more.

In Figure 7, we show the corresponding coherence distributions for the three time steps. Within the branching region (see Figures 7B and 7E), FSSH-wf exhibits an erroneous long-range oscillation pattern for $x > -1$ because the wavefunctions of transmitted trajectories retain overcoherent. With branching correction, both BCSH-wf and BCSH-cc eliminate the oscillations and give more accurate oscillating phases of the coherence distribution. In particular, BCSH-cc produces more accurate oscillating amplitudes. After trajectory branching at $t = 4200$ au, both BCSH-wf and BCSH-cc can recover the exact quantum results. For FSSH-wf, the results are completely wrong, and residual oscillations are still present in the transmission region.

We choose $k_0 = 30$ au as a representative high-energy case for the ECR model. As the kinetic energy is large enough, the WP on the upper PES can overcome the barrier such that trajectory branching does not occur. In Figure 8, we show the time evolution of population distributions. Despite the absence of strong branching events, correctly characterizing the slow WP splitting is still important. When the WP enters the branching region at $t = 1000$ au, the wavefunction-based methods begin to deviate from the exact results due to the lack of decoherence (see Figures 8A and 8D). The population

peaks by both FSSH-wf and BCSH-wf are located at the same positions on the upper and lower PESs, while the population distribution by BCSH-as properly depicts the slight separation of population peaks on the two adiabatic PESs. After the WP on the upper PES overcomes the barrier (e.g., t = 1400 and 1800 au), the fully quantum dynamics still exhibits only one single peak on each PES, but FSSH-wf and BCSH-wf show two peaks on both upper and lower PESs due to overcoherent propagation of the electronic wavefunction. In contrast, BCSH-as exhibits accurate distributions, as active states of the trajectory ensemble could capture the slow splitting of WPs.

In Figure 9, we show time evolution of the coherence distribution. At t = 1400 au, both FSSH-wf and BCSH-wf fail to capture the slow decoherence and produce incorrect oscillation peaks. BCSH-wf even gives more severe oscillations compared to those of FSSH-wf. This stems from the phase correction, which has shown enhanced oscillating patterns of the branching ratios in previous studies.[84] After the WP on the upper PES overcomes the barrier, the coherence distribution by BCSH-wf maintains the incorrect oscillating pattern due to the phase correction, whereas FSSH-wf eliminates the oscillating pattern by averaging the phases of electronic wavefunctions from different trajectories.[94] In comparison, BCSH-cc always gives correct results.

In Figure 10, we show the time evolution of population on the upper PES and the indicator of coherence constructed by different methods at the two initial momenta. In the low-energy case with k_0 = 10 au (see Figures 10A and 10C), FSSH begins to deviate notably from the exact quantum results when the reflected WP component on the upper PES reenters the interaction region. The overcoherent wavefunction generated by FSSH

results in incorrect hopping probabilities between the two adiabatic states, leading to some errors for the reduced density matrix even if it is constructed consistently. CT-MQC is able to approximately predict the asymptotic population and indicator of coherence, but there are notable deviations during the dynamics. In comparison, BCSH-cc perfectly recovers the exact results for both population and indicator of coherence. The results of the high-energy case with k_0 = 30 au are shown in Figures 10B and 10D. Both FSSH-cc and BCSH-cc recover the exact results. While the population calculated by CT-MQC is satisfactory, the corresponding indicator of coherence begins to deviate from the reference when t > 800 au, exhibiting too fast decoherence.

C. The STD Model

The STD model was proposed by Subotnik to quantify the decoherence effects in multidimensional cases.[88] We choose the initial conditions as x_0 = -4, y_0 = 0, k_x = 10, k_y = 0 and place the WP on the upper PES to investigate the performance of our consistent method to construct the density matrix in multidimensional systems. According to the exact quantum results obtained by DVR, we can identify important branching events and generation of WPs during the dynamics (see Figure 11). At t = 1000 au, the initial WP labeled with 1 (i.e., WP-1) on the upper PES enters the interaction region and gets reflected, generating WP-2 and WP-3 on the lower PES (see Figure 11E). Along with the reflection of WP-1 on the upper PES, WP-2 gets transmitted on the lower PES. This is the first branching event, following which WP-1 and WP-3 move together. At t = 1450 au, WP-1 and WP-3 reach the next turning point and are scattered by the barrier for the second time, while generating WP-4 and WP-5 on the lower PES (see Figures

11F and 11G). After t = 2300 au, WP-3 and WP-4 are scattered by the barrier on the lower PES, while WP-5 continues to move along with WP-1 and the second branching event is completed (see Figures 11D and 11H).

In Figure 12, we show the real parts of the coherence distributions constructed by FSSH-wf, BCSH-wf, FSSH-cc and BCSH-cc methods at the corresponding time steps. The results of the corresponding imaginary parts are shown in the SI. At t = 1000 au (see Figures 12A-12E), the coherence is produced by the overlap between WP-1 and WP-3. Due to the inherent lack of decoherence in FSSH-wf, more trajectories hop incorrectly from the upper PES to the lower PES, which leads to incorrect coherence distribution in the region of $-3 < x < -1$. With the branching correction, the incorrect coherence distribution is significantly reduced in BCSH-wf. In addition, the coherence fringes are also much closer to the quantum reference due to the phase correction. As WP-1 reaches the second turning point and generates WP-4 and WP-5, WP-3 is scattered away such that the major coherence distribution emerges from the overlap between WP-1 and the newly generated WP-4 (see Figures 12F and 12K). Since WP-3 produced by FSSH-wf is incorrect (see details in the SI), the overlap between WP-1 and WP-3 results in erroneous behavior on the left side of the main coherence distribution (see Figures 12G and 12L). The second branching event takes place as WP-4 gradually separates with WP-1. FSSH-wf cannot correctly describe this branching event either, resulting in additional incorrect behavior on the right side of the main coherence distribution (see Figure 12L). Again, BCSH-wf eliminates the incorrect coherence distribution in FSSH-wf and also gives more accurate coherence fringes (see

Figures 12H and 12M). After the second branching event, WP-3 and WP-4 leave WP-1, and the coherence is produced by the overlap between WP-1 and the newly generated WP-5. Due to the incorrect WP-3, FSSH-wf still maintains erroneous distribution on the top-left part of the coherence distribution. Moreover, the main coherence fringes also deviate significantly from the quantum reference. In comparison, BCSH-wf eliminates the incorrect top-left part and produces more accurate stripes in the main part of the coherent distribution. With our consistent construction of density matrix, even the results obtained from FSSH trajectories demonstrate significant improvement (see Figures 12D, 12I, 12N and 12S). In particular, BCSH-cc gives highly accurate coherence distributions and fringes compared with the exact results (see Figures 12E, 12J, 12O and 12T). These results indicate that if proper decoherence and density matrix construction methods are utilized, coherence produced by surface hopping dynamics can also exhibit a high level of accuracy for complex systems.

4. CONCLUSIONS

In summary, we have proposed a consistent method to construct the density matrix for surface hopping simulations. Both population and coherence distributions have been obtained. In particular, the occupation of active states and the electronic wavefunction have been utilized to define the amplitude and phase of coherence, respectively. It has been shown that the separation of WPs on different adiabatic PESs can be properly captured by the adiabatic nuclear dynamics on the active PES, and thus the occupation of active states is more reliable than the electronic wavefunction when analyzing the adiabatic populations. Utilizing this advantage, our consistent construction method has

significantly improved the performance even using traditional FSSH trajectories as demonstrations. Most importantly, the consistently constructed density matrix from BCSH trajectories has shown highly accurate results in representative one- and two-dimensional scattering models.

In terms of future prospects, we need to build a general and efficient decoherence scheme to obtain more accurate electronic wavefunction in surface hopping dynamics, instead of relying on active states of the trajectory ensemble. Such a self-consistent method will significantly extend the applicability of surface hopping to spectroscopy and related studies.[95-98] Within the independent trajectory framework, however, it is not easy to get correct wavefunctions because WP branching events can only be depicted by more than one trajectory. Recently, we have proposed a new mean field method based on auxiliary trajectories on adiabatic PESs, which gives the correct spatial distribution of population.[99] It is natural to adopt this strategy in surface hopping as adiabatic dynamics is intrinsically embedded. These studies are currently under way.

AUTHOR INFORMATION

[#]These authors contributed equally to this work.

Corresponding Author

*Email: ljwang@zju.edu.cn

Author Contributions

The manuscript was written through contributions of all authors. All authors have given approval to the final version of the manuscript.

Notes

The authors declare no competing financial interest.

ACKNOWLEDGMENTS

L.W. acknowledges support from the National Natural Science Foundation of China (Grant Nos. 22273082 and 21922305) and the High-Performance Computing Center in Department of Chemistry, Zhejiang University.

ASSOCIATED CONTENT

Supporting Information

We give the computational details, Hamiltonians of the investigated models, additional results for the one- and two-dimensional models, and supplementary figures.

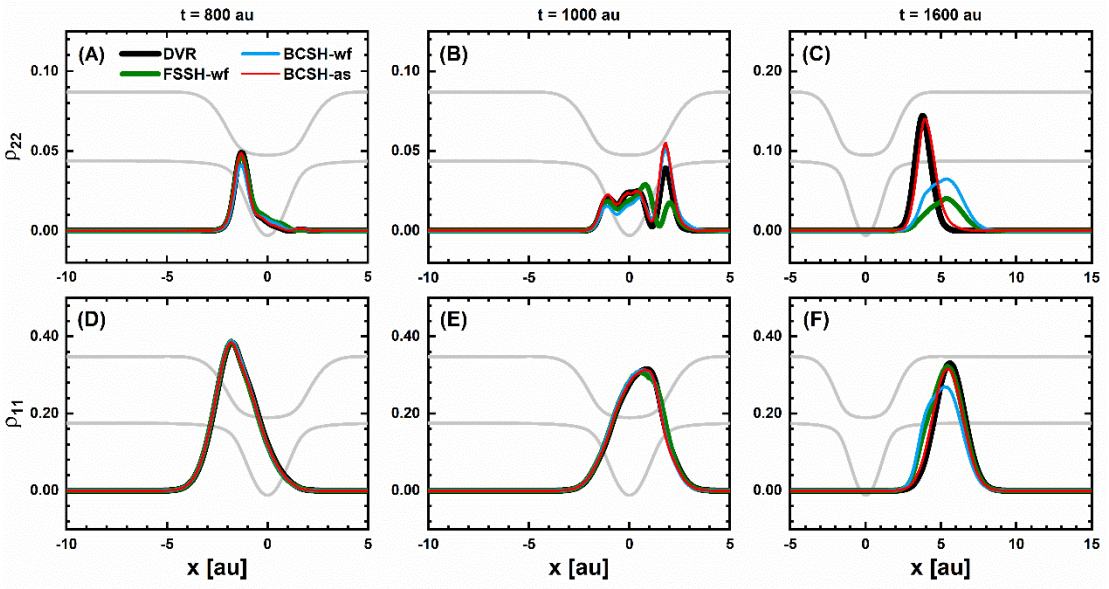

Figure 1. Population distribution on the (A-C) upper and (D-F) lower adiabatic PESs at three different time for the DAC model. The initial momentum is set as $k_0 = 16$ au. The black lines represent the exact quantum dynamics with DVR. The results by FSSH-wf, BCSH-wf and BCSH-as are shown as green, light blue, and red lines, respectively. The upper and lower adiabatic PESs are shown by grey lines. (A, D), (B, E) and (C, F) correspond to $t = 800$, 1000 and 1600 au, respectively.

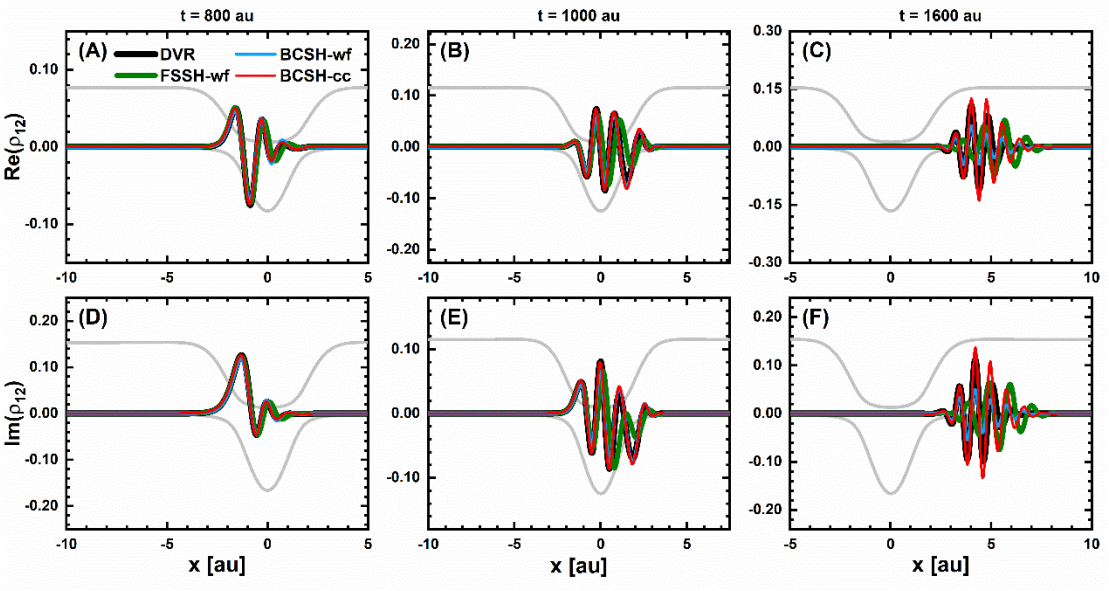

Figure 2. (A-C) Real and (D-F) imaginary parts of the coherence distribution at three different time for the DAC model. The initial momentum is set as $k_0 = 16$ au. The black lines represent the exact quantum dynamics with DVR. The results by FSSH-wf, BCSH-wf and BCSH-cc are shown as green, light blue, and red lines, respectively. The upper and lower adiabatic PESs are shown by grey lines. (A, D), (B, E) and (C, F) correspond to $t = 800$, 1000 and 1600 au, respectively.

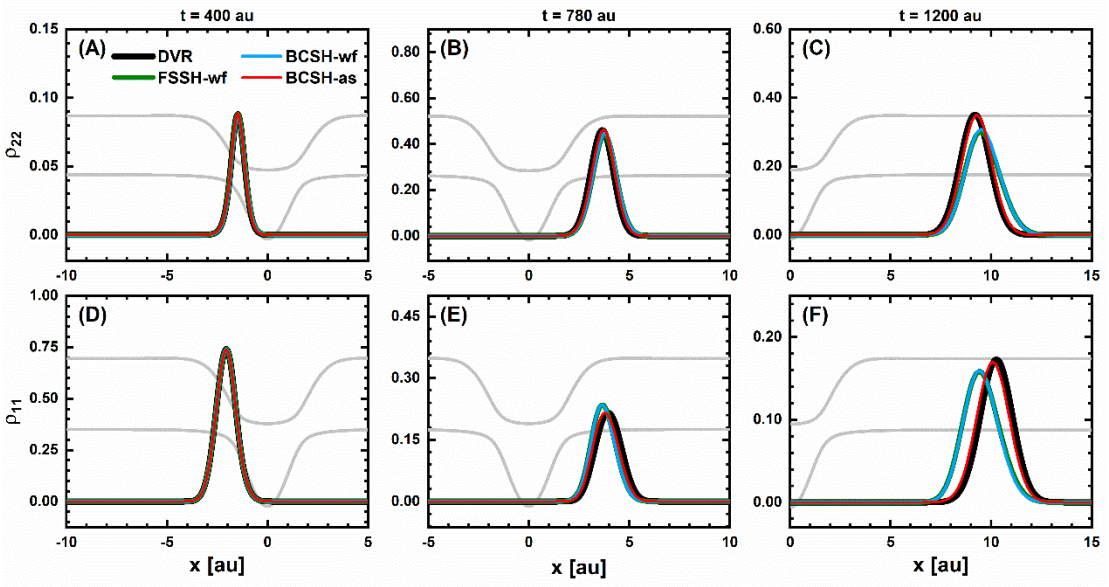

Figure 3. Population distribution on the (A-C) upper and (D-F) lower PESs at three different time for the DAC model. The initial momentum is set as $k_0 = 30$ au. The line colors are the same as those in Figure 1. (A, D), (B, E) and (C, F) correspond to $t = 400$, 780 and 1200 au, respectively.

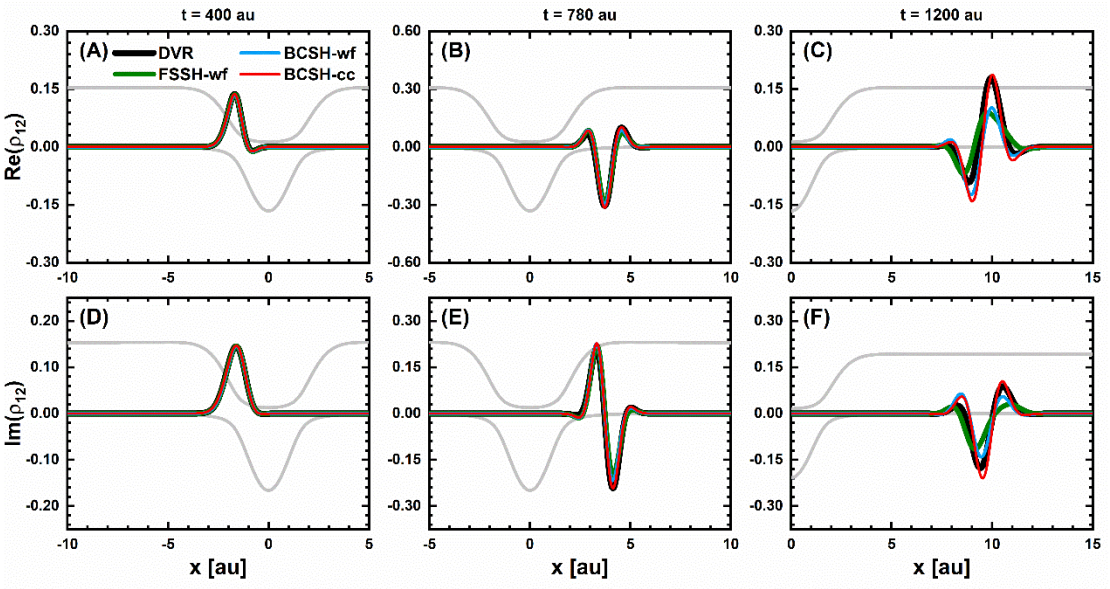

Figure 4. (A-C) Real and (D-F) imaginary parts of the coherence distribution at three different time for the DAC model. The initial momentum is set as $k_0 = 30$ au. The line colors are the same as those in Figure 2. (A, D), (B, E) and (C, F) correspond to $t = 400$, 780 and 1200 au, respectively.

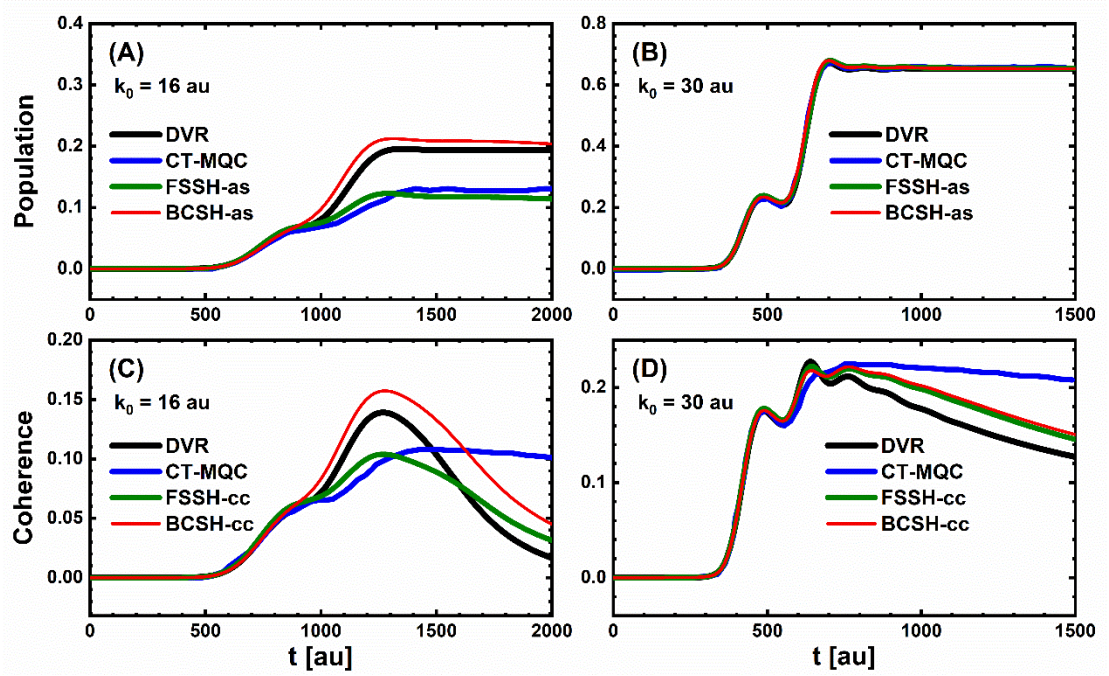

Figure 5. Time-dependent (A, B) population on the upper adiabatic PES and (C, D) indicator of coherence for the DAC model. The initial momenta are k_0 = 16 and 30 au for (A, C) and (B, D), respectively. The black lines represent the exact quantum dynamics with DVR. The results of CT-MQC are adopted from Ref. 32 and plotted as blue lines. The results of FSSH-as and FSSH-cc are shown as green lines, and those of BCSH-as and BCSH-cc are shown as red lines.

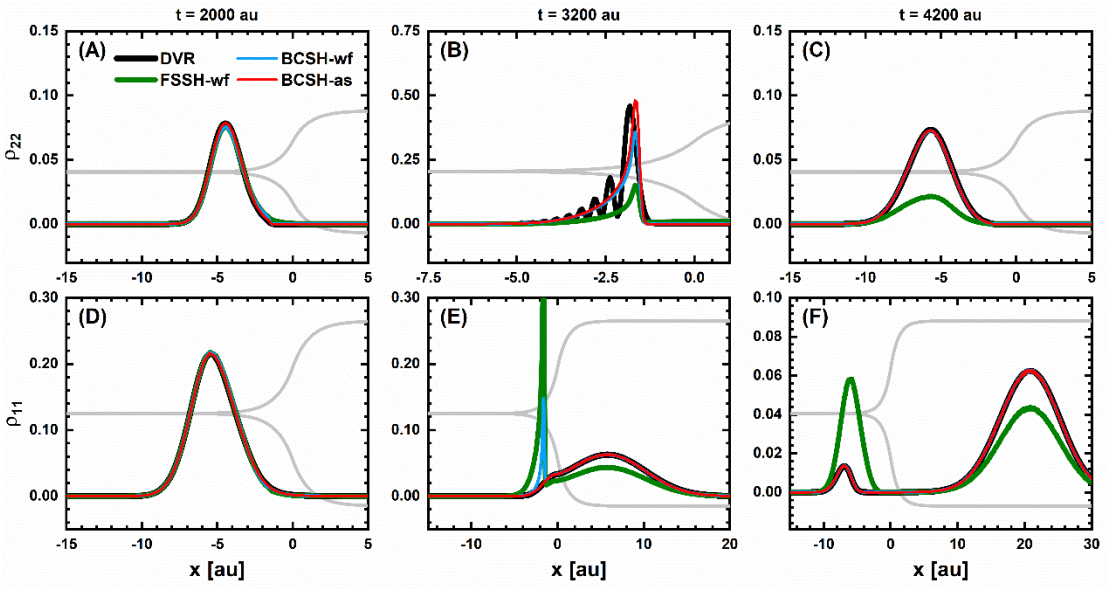

Figure 6. Population distribution on the (A-C) upper and (D-F) lower adiabatic PESs at three different time for the ECR model. The initial momentum is set as $k_0 = 10$ au. The line colors are the same as those in Figure 1. (A, D), (B, E) and (C, F) correspond to $t = 2000$, 3200 and 4200 au, respectively.

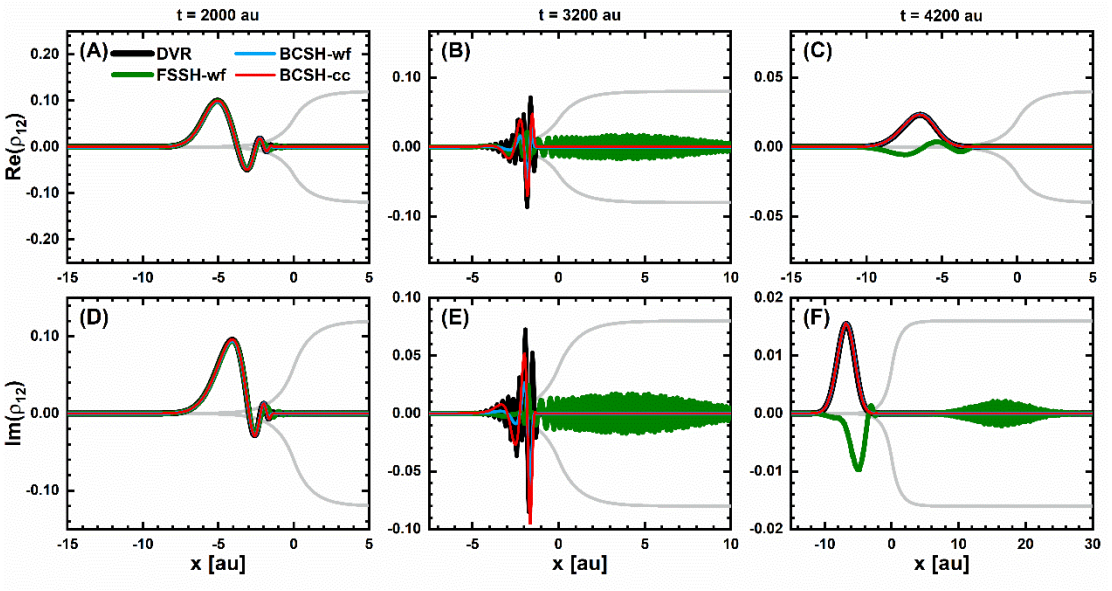

Figure 7. (A-C) Real and (D-F) imaginary parts of the coherence distribution at three different time for the ECR model. The initial momentum is set as $k_0 = 10$ au. The line colors are the same as those in Figure 2. (A, D), (B, E) and (C, F) correspond to t = 2000, 3200 and 4200 au, respectively.

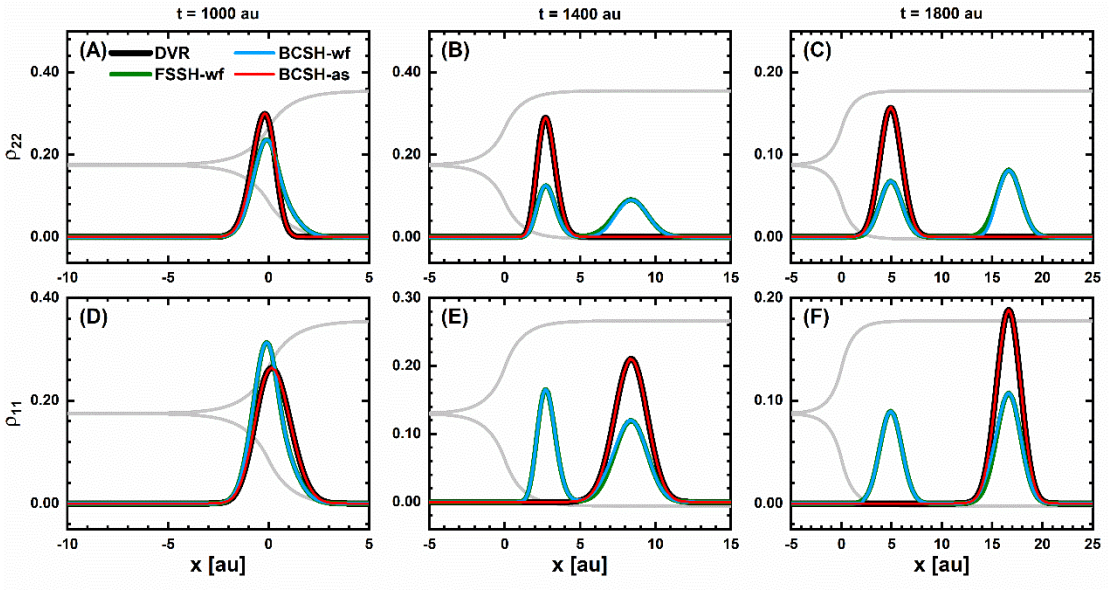

Figure 8. Population distribution on the (A-C) upper and (D-F) lower adiabatic PESs at three different time for the ECR model. The initial momentum is set as $k_0 = 30$ au. The line colors are the same as those in Figure 1. (A, D), (B, E) and (C, F) correspond to $t = 1000$, 1400 and 1800 au, respectively.

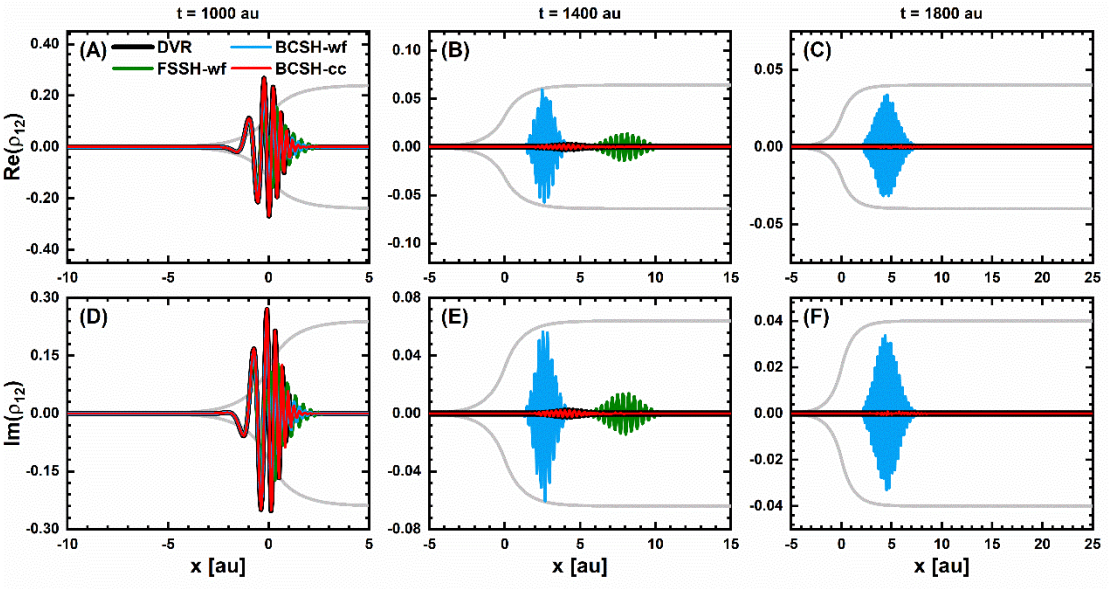

Figure 9. (A-C) Real and (D-F) imaginary parts of the coherence distribution at three different time for the ECR model. The initial momentum is set as $k_0 = 30$ au. The line colors are the same as those in Figure 2. (A, D), (B, E) and (C, F) correspond to t = 1000, 1400 and 1800 au, respectively.

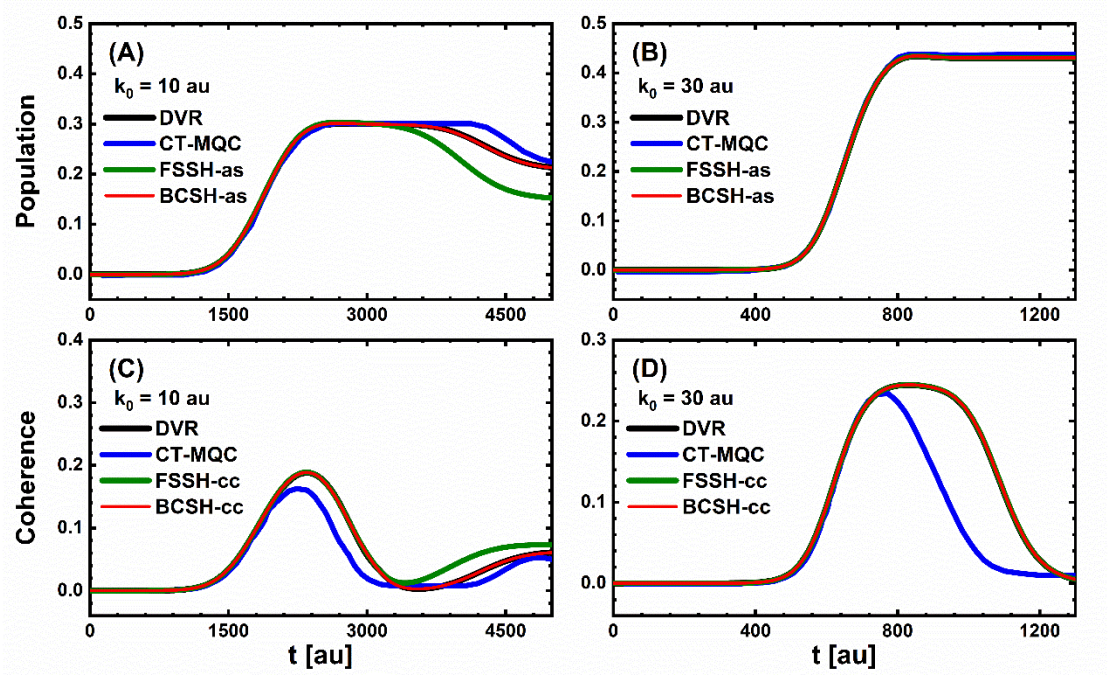

Figure 10. Time-dependent (A, B) population on the upper adiabatic PES and (C, D) indicator of coherence for the ECR model. The initial momenta are k_0 = 10 and 30 au for (A, C) and (B, D), respectively. The line colors are the same as those in Figure 5.

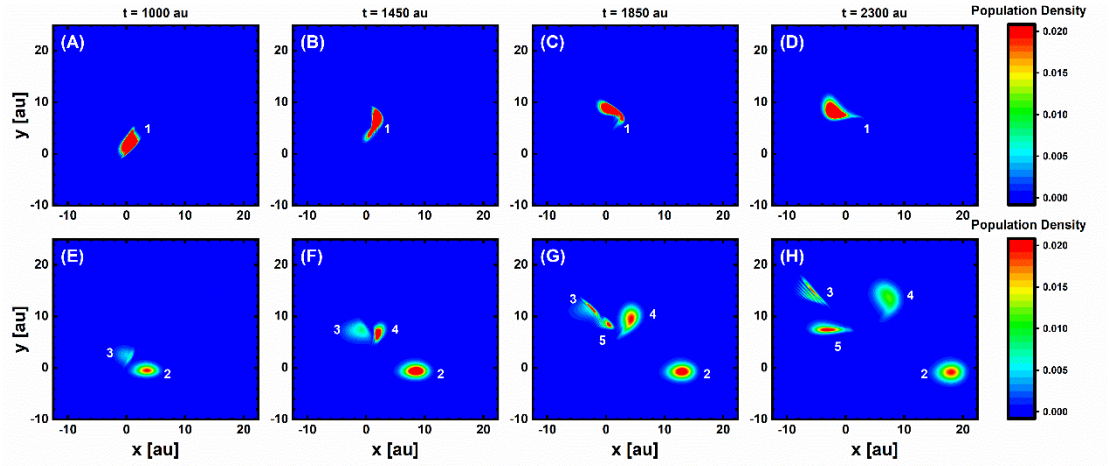

Figure 11. Population distribution on the (A-D) upper and (E-H) lower adiabatic PESs of the STD model obtained by the exact quantum dynamics with DVR. The initial conditions are x_0 = -4, y_0 = 0, k_x = 10 and k_y = 0. (A, E), (B, F), (C, G) and (D, H) correspond to t = 1000, 1450, 1850 and 2300 au, respectively. The labels 1, 2, 3, 4 and 5 indicate WP-1, WP-2, WP-3, WP-4 and WP-5, respectively.

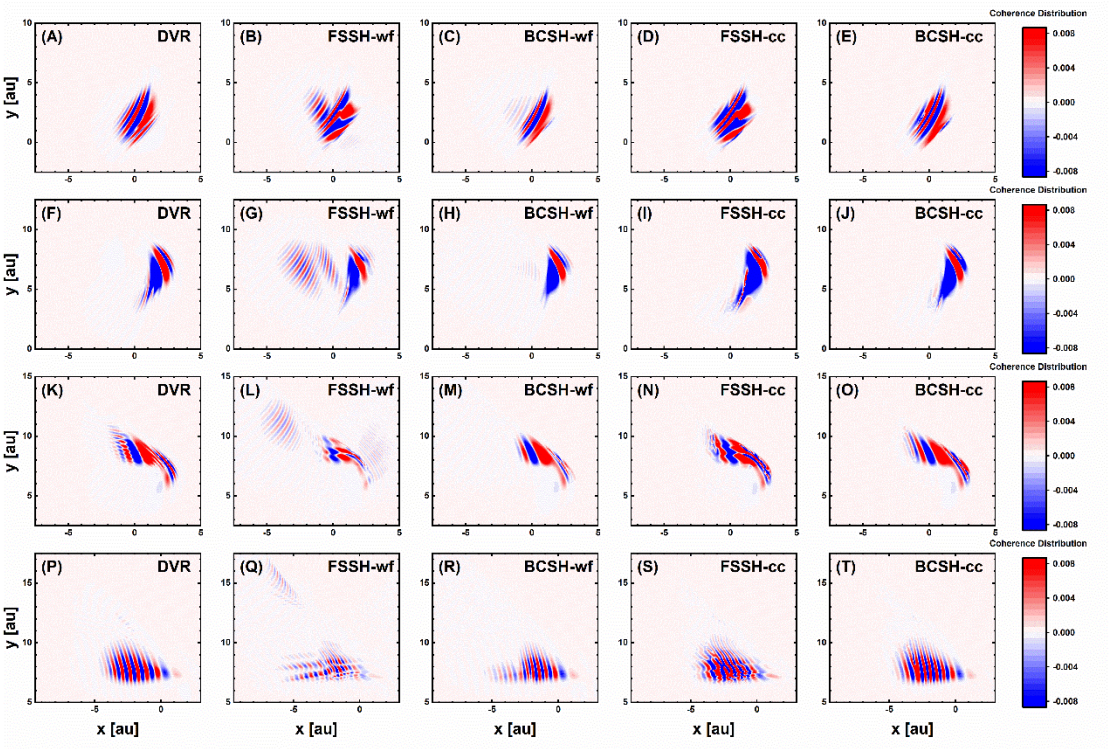

Figure 12. Real part of the coherence distribution obtained by (A, F, K and P) DVR, (B, G, L and Q) FSSH-wf, (C, H, M and R) BCSH-wf, (D, I, N and S) FSSH-cc and (E, J, O and T) BCSH-cc. The initial conditions are x_0 = -4, y_0 = 0, k_x = 10 and k_y = 0. (A-E), (F-J), (K-O) and (P-T) correspond to t = 1000, 1450, 1850 and 2300 au, respectively.

REFERENCES

(1) Hammes-Schiffer, S.; Tully, J. C. Proton Transfer in Solution: Molecular Dynamics with Quantum Transitions. *J. Chem. Phys.* **1994**, *101*, 4657–4667.

(2) Chen, L.; Shi, Q. Quantum Rate Dynamics for Proton Transfer Reactions in Condensed Phase: The Exact Hierarchical Equations of Motion Approach. *J. Chem. Phys.* **2009**, *130*, 134505.

(3) Song, K.; Shi, Q. Theoretical Study of Photoinduced Proton Coupled Electron Transfer Reaction Using the Non-Perturbative Hierarchical Equations of Motion Method. *J. Chem. Phys.* **2017**, *146*, 184108.

(4) Ke, Y.; Kaspar, C.; Erpenbeck, A.; Peskin, U.; Thoss, M. Nonequilibrium Reaction Rate Theory: Formulation and Implementation within the Hierarchical Equations of Motion Approach. *J. Chem. Phys.* **2022**, *157*, 034103.

(5) Sun, J.; Luo, B.; Zhao, Y. Dynamics of a One-Dimensional Holstein Polaron with the Davydov Ansätze. *Phys. Rev. B* **2010**, *82*, 014305.

(6) Chen, L.; Zhao, Y.; Tanimura, Y. Dynamics of a One-Dimensional Holstein Polaron with the Hierarchical Equations of Motion Approach. *J. Phys. Chem. Lett.* **2015**, *6*, 3110–3115.

(7) Chen, L.; Zhao, Y. Finite Temperature Dynamics of a Holstein Polaron: The Thermo-Field Dynamics Approach. *J. Chem. Phys.* **2017**, *147*, 214102.

(8) Chen, L.; Gelin, M. F.; Shalashilin, D. V. Dynamics of a One-Dimensional Holstein Polaron: The Multiconfigurational Ehrenfest Method. *J. Chem. Phys.* **2019**, *151*, 244116.

(9) Liu, X. Y.; Li, Z. W.; Fang, W. H.; Cui, G. Nonadiabatic Exciton and Charge Separation Dynamics at Interfaces of Zinc Phthalocyanine and Fullerene: Orientation Does Matter. *J. Phys. Chem. A* **2020**, *124*, 7388–7398.

(10) Jiang, X.; Zheng, Q.; Lan, Z.; Saidi, W. A.; Ren, X.; Zhao, J. Real-Time GW-BSE Investigations on Spin-Valley Exciton Dynamics in Monolayer Transition Metal Dichalcogenide. *Sci. Adv.* **2021**, *7*, eabf3759.

(11) Liu, J.; Zhang, X.; Lu, G. Non-Adiabatic Exciton Dynamics in van der Waals Heterostructures. *J. Phys. Chem. Lett.* **2022**, *13*, 11760–11769.

(12) Guo, H.; Zhang, X.; Lu, G. Tuning Moiré Excitons in Janus Heterobilayers for High-Temperature Bose-Einstein Condensation. *Sci. Adv.* **2022**, *8*, eabp9757.

(13) Müller, U.; Stock, G. Surface-Hopping Modeling of Photoinduced Relaxation Dynamics on Coupled Potential-Energy Surfaces. *J. Chem. Phys.* **1997**, *107*, 6230–6245.

(14) Feynman, R. P. Space-Time Approach to Non-Relativistic Quantum Mechanics. *Rev. Mod. Phys.* **1948**, *20*, 367–387.

(15) Feynman, R. P.; Hibbs, A. R. *Quantum Mechanics and Path Integrals*. McGraw-Hill, New York, 1965.

(16) Heller, E. J. Cellular Dynamics: A New Semiclassical Approach to Time-Dependent Quantum Mechanics. *J. Chem. Phys.* **1991**, *94*, 2723–2729.

(17) Kay, K. G. Numerical Study of Semiclassical Initial Value Methods for Dynamics. *J. Chem. Phys.* **1994**, *100*, 4432–4445.

(18) Kay, K. G. Integral Expressions for the Semiclassical Time-Dependent

Propagator. *J. Chem. Phys.* **1994**, *100*, 4377–4392.

(19) Wang, H.; Sun, X.; Miller, W. H. Semiclassical Approximations for the Calculation of Thermal Rate Constants for Chemical Reactions in Complex Molecular Systems. *J. Chem. Phys.* **1998**, *108*, 9726–9736.

(20) Sun, X.; Wang, H.; Miller, W. H. Semiclassical Theory of Electronically Nonadiabatic Dynamics: Results of a Linearized Approximation to the Initial Value Representation. *J. Chem. Phys.* **1998**, *109*, 7064–7074.

(21) Miller, W. H. The Semiclassical Initial Value Representation: A Potentially Practical Way for Adding Quantum Effects to Classical Molecular Dynamics Simulations. *J. Phys. Chem. A* **2001**, *105*, 2942–2955.

(22) Miller, W. H. Perspective: Quantum or Classical Coherence? *J. Chem. Phys.* **2012**, *136*, 210901.

(23) Mak, C. H.; Chandler, D. Solving the Sign Problem in Quantum Monte Carlo Dynamics. *Phys. Rev. A* **1990**, *41*, 5709–5712.

(24) Cohen, G.; Gull, E.; Reichman, D. R.; Millis, A. J. Taming the Dynamical Sign Problem in Real-Time Evolution of Quantum Many-Body Problems. *Phys. Rev. Lett.* **2015**, *115*, 266802.

(25) Church, M. S.; Ananth, N. Semiclassical Dynamics in the Mixed Quantum-Classical Limit. *J. Chem. Phys.* **2019**, *151*, 134109.

(26) Meyer, H. D.; Miller, W. H. A Classical Analog for Electronic Degrees of Freedom in Nonadiabatic Collision Processes. *J. Chem. Phys.* **1979**, *70*, 3214–3223.

(27) Stock, G.; Thoss, M. Semiclassical Description of Nonadiabatic Quantum

Dynamics. *Phys. Rev. Lett.* **1997**, *78*, 578–581.

(28) Abedi, A.; Maitra, N. T.; Gross, E. K. U. Exact Factorization of the Time-Dependent Electron-Nuclear Wave Function. *Phys. Rev. Lett.* **2010**, *105*, 123002.

(29) Gorshkov, V. N.; Tretiak, S.; Mozyrsky, D. Semiclassical Monte-Carlo Approach for Modelling Non-Adiabatic Dynamics in Extended Molecules. *Nat. Commun.* **2013**, *4*, 2144.

(30) White, A. J.; Gorshkov, V. N.; Wang, R.; Tretiak, S.; Mozyrsky, D. Semiclassical Monte Carlo: A First Principles Approach to Non-Adiabatic Molecular Dynamics. *J. Chem. Phys.* **2014**, *141*, 184101.

(31) Min, S. K.; Agostini, F.; Gross, E. K. U. Coupled-Trajectory Quantum-Classical Approach to Electronic Decoherence in Nonadiabatic Processes. *Phys. Rev. Lett.* **2015**, *115*, 073001.

(32) Agostini, F.; Min, S. K.; Abedi, A.; Gross, E. K. U. Quantum-Classical Nonadiabatic Dynamics: Coupled- vs Independent-Trajectory Methods. *J. Chem. Theory Comput.* **2016**, *12*, 2127–2143.

(33) White, A. J.; Gorshkov, V. N.; Tretiak, S.; Mozyrsky, D. Non-Adiabatic Molecular Dynamics by Accelerated Semiclassical Monte Carlo. *J. Chem. Phys.* **2015**, *143*, 014115.

(34) Liu, J. A Unified Theoretical Framework for Mapping Models for the Multi-State Hamiltonian. *J. Chem. Phys.* **2016**, *145*, 204105.

(35) Liu, J. Isomorphism between the Multi-State Hamiltonian and the Second-Quantized Many-Electron Hamiltonian with Only 1-Electron Interactions. *J. Chem.*

Phys. **2017**, *146*, 024110.

(36) Runeson, J. E.; Richardson, J. O. Spin-Mapping Approach for Nonadiabatic Molecular Dynamics. *J. Chem. Phys.* **2019**, *151*, 044119.

(37) Runeson, J. E.; Richardson, J. O. Generalized Spin Mapping for Quantum-Classical Dynamics. *J. Chem. Phys.* **2020**, *152*, 084110.

(38) Liu, J.; He, X.; Wu, B. Unified Formulation of Phase Space Mapping Approaches for Nonadiabatic Quantum Dynamics. *Acc. Chem. Res.* **2021**, *54*, 4215–4228.

(39) He, X.; Wu, B.; Shang, Y.; Li, B.; Cheng, X.; Liu, J. New Phase Space Formulations and Quantum Dynamics Approaches. *Wiley Interdiscip. Rev. Comput. Mol. Sci.* **2022**, *12*, e1619.

(40) Sun, X.; Miller, W. H. Semiclassical Initial Value Representation for Electronically Nonadiabatic Molecular Dynamics. *J. Chem. Phys.* **1997**, *106*, 6346–6353.

(41) Hele, T. J. H.; Ananth, N. Deriving the Exact Nonadiabatic Quantum Propagator in the Mapping Variable Representation. *Faraday Discuss.* **2016**, *195*, 269–289.

(42) He, X.; Liu, J. A New Perspective for Nonadiabatic Dynamics with Phase Space Mapping Models. *J. Chem. Phys.* **2019**, *151*, 024105.

(43) Mannouch, J. R.; Richardson, J. O. A Partially Linearized Spin-Mapping Approach for Nonadiabatic Dynamics. I. Derivation of the Theory. *J. Chem. Phys.* **2020**, *153*, 194109.

(44) Mannouch, J. R.; Richardson, J. O. A Partially Linearized Spin-Mapping

Approach for Nonadiabatic Dynamics. II. Analysis and Comparison with Related Approaches. *J. Chem. Phys.* **2020**, *153*, 194110.

(45) Gao, X.; Saller, M. A. C.; Liu, Y.; Kelly, A.; Richardson, J. O.; Geva, E. Benchmarking Quasiclassical Mapping Hamiltonian Methods for Simulating Electronically Nonadiabatic Molecular Dynamics. *J. Chem. Theory Comput.* **2020**, *16*, 2883–2895.

(46) He, X.; Wu, B.; Gong, Z.; Liu, J. Commutator Matrix in Phase Space Mapping Models for Nonadiabatic Quantum Dynamics. *J. Phys. Chem. A* **2021**, *125*, 6845–6863.

(47) He, X.; Gong, Z.; Wu, B.; Liu, J. Negative Zero-Point-Energy Parameter in the Meyer-Miller Mapping Model for Nonadiabatic Dynamics. *J. Phys. Chem. Lett.* **2021**, *12*, 2496–2501.

(48) Min, S. K.; Agostini, F.; Tavernelli, I.; Gross, E. K. U. Ab Initio Nonadiabatic Dynamics with Coupled Trajectories: A Rigorous Approach to Quantum (De)Coherence. *J. Phys. Chem. Lett.* **2017**, *8*, 3048–3055.

(49) Ha, J. K.; Lee, I. S.; Min, S. K. Surface Hopping Dynamics beyond Nonadiabatic Couplings for Quantum Coherence. *J. Phys. Chem. Lett.* **2018**, *9*, 1097–1104.

(50) Pieroni, C.; Agostini, F. Nonadiabatic Dynamics with Coupled Trajectories. *J. Chem. Theory Comput.* **2021**, *17*, 5969–5991.

(51) Dupuy, L.; Talotta, F.; Agostini, F.; Lauvergnat, D.; Poirier, B.; Scribano, Y. Adiabatic and Nonadiabatic Dynamics with Interacting Quantum Trajectories. *J. Chem. Theory Comput.* **2022**, *18*, 6447–6462.

(52) Ha, J. K.; Min, S. K. Independent Trajectory Mixed Quantum-Classical

Approaches Based on the Exact Factorization. *J. Chem. Phys.* **2022**, *156*, 174109.

(53) Tully, J. C. Molecular Dynamics with Electronic Transitions. *J. Chem. Phys.* **1990**, *93*, 1061–1071.

(54) Tully, J. C. Perspective: Nonadiabatic Dynamics Theory. *J. Chem. Phys.* **2012**, *137*, 22A301.

(55) Sholl, D. S.; Tully, J. C. A Generalized Surface Hopping Method. *J. Chem. Phys.* **1998**, *109*, 7702–7710.

(56) Fang, J. Y.; Hammes-Schiffer, S. Comparison of Surface Hopping and Mean Field Approaches for Model Proton Transfer Reactions. *J. Chem. Phys.* **1999**, *110*, 11166–11175.

(57) Parandekar, P. V.; Tully, J. C. Mixed Quantum-Classical Equilibrium. *J. Chem. Phys.* **2005**, *122*, 094102.

(58) ten Brink, M.; Gräber, S.; Hopjan, M.; Jansen, D.; Stolpp, J.; Heidrich-Meisner, F.; Blöchl, P. E. Real-Time Non-Adiabatic Dynamics in the One-Dimensional Holstein Model: Trajectory-Based vs Exact Methods. *J. Chem. Phys.* **2022**, *156*, 234109.

(59) Bittner, E. R.; Rossky, P. J. Quantum Decoherence in Mixed Quantum-Classical Systems: Nonadiabatic Processes. *J. Chem. Phys.* **1995**, *103*, 8130–8143.

(60) Chen, H. T.; Reichman, D. R. On the Accuracy of Surface Hopping Dynamics in Condensed Phase Non-Adiabatic Problems. *J. Chem. Phys.* **2016**, *144*, 094104.

(61) Bai, X.; Qiu, J.; Wang, L. J. An Efficient Solution to the Decoherence Enhanced Trivial Crossing Problem in Surface Hopping. *J. Chem. Phys.* **2018**, *148*, 104106.

(62) Qiu, J.; Bai, X.; Wang, L. J. Crossing Classified and Corrected Fewest Switches

Surface Hopping. *J. Phys. Chem. Lett.* **2018**, *9*, 4319–4325.

(63) Tempelaar, R.; Reichman, D. R. Generalization of Fewest-Switches Surface Hopping for Coherences. *J. Chem. Phys.* **2018**, *148*, 102309.

(64) Martens, C. C. Classical and Nonclassical Effects in Surface Hopping Methodology for Simulating Coupled Electronic-Nuclear Dynamics. *Faraday Discuss.* **2020**, *221*, 449–477.

(65) Qiu, J.; Bai, X.; Wang, L. J. Subspace Surface Hopping with Size-Independent Dynamics. *J. Phys. Chem. Lett.* **2019**, *10*, 637–644.

(66) Miao, G.; Subotnik, J. Revisiting the Recoherence Problem in the Fewest Switches Surface Hopping Algorithm. *J. Phys. Chem. A* **2019**, *123*, 5428–5435.

(67) Wang, L. J.; Qiu, J.; Bai, X.; Xu, J. B. Surface Hopping Methods for Nonadiabatic Dynamics in Extended Systems. *Wiley Interdiscip. Rev. Comput. Mol. Sci.* **2020**, *10*, e1435.

(68) Shenvi, N.; Subotnik, J. E.; Yang, W. Simultaneous-Trajectory Surface Hopping: A Parameter-Free Algorithm for Implementing Decoherence in Nonadiabatic Dynamics. *J. Chem. Phys.* **2011**, *134*, 144102.

(69) Jaeger, H. M.; Fischer, S.; Prezhdo, O. V. Decoherence-Induced Surface Hopping. *J. Chem. Phys.* **2012**, *137*, 22A545.

(70) Subotnik, J. E.; Jain, A.; Landry, B.; Petit, A.; Ouyang, W.; Bellonzi, N. Understanding the Surface Hopping View of Electronic Transitions and Decoherence. *Annu. Rev. Phys. Chem.* **2016**, *67*, 387–417.

(71) Sindhu, A.; Jain, A. An Efficient Decoherence Scheme for Fewest Switches

Surface Hopping Method. *J. Chem. Phys.* **2023**, *158*, 154109.

(72) Schmidt, J. R.; Parandekar, P. V.; Tully, J. C. Mixed Quantum-Classical Equilibrium: Surface Hopping. *J. Chem. Phys.* **2008**, *129*, 044104.

(73) Jasper, A. W.; Stechmann, S. N.; Truhlar, D. G. Fewest-Switches with Time Uncertainty: A Modified Trajectory Surface-Hopping Algorithm with Better Accuracy for Classically Forbidden Electronic Transitions. *J. Chem. Phys.* **2002**, *116*, 5424–5431.

(74) Granucci, G.; Persico, M. Critical Appraisal of the Fewest Switches Algorithm for Surface Hopping. *J. Chem. Phys.* **2007**, *126*, 134114.

(75) Xiao, B. Y.; Xu, J. B.; Wang, L. J. New Energy-Based Decoherence Correction Approaches for Trajectory Surface Hopping. *Chinese J. Chem. Phys.* **2020**, *33*, 603–612.

(76) Shao, C. C.; Shi, Z. C; Xu, J. B.; Wang, L. J. Learning Decoherence Time Formulas for Surface Hopping from Quantum Dynamics. *J. Phys. Chem. Lett.* **2023**, *14*, 7680–7689.

(77) Subotnik, J. E.; Shenvi, N. A New Approach to Decoherence and Momentum Rescaling in the Surface Hopping Algorithm. *J. Chem. Phys.* **2011**, *134*, 024105.

(78) Landry, B. R.; Subotnik, J. E. How to Recover Marcus Theory with Fewest Switches Surface Hopping: Add Just a Touch of Decoherence. *J. Chem. Phys.* **2012**, *137*, 22A513.

(79) Martens, C. C.; Fang, J. Y. Semiclassical-Limit Molecular Dynamics on Multiple Electronic Surfaces. *J. Chem. Phys.* **1997**, *106*, 4918–4930.

(80) Kapral, R.; Ciccotti, G. Mixed Quantum-Classical Dynamics. *J. Chem. Phys.*

1999, *110*, 8919–8929.

(81) Nielsen, S.; Kapral, R.; Ciccotti, G. Mixed Quantum-Classical Surface Hopping Dynamics. *J. Chem. Phys.* **2000**, *112*, 6543–6553.

(82) Subotnik, J. E.; Ouyang, W.; Landry, B. R. Can We Derive Tully's Surface-Hopping Algorithm from the Semiclassical Quantum Liouville Equation? Almost, but Only with Decoherence. *J. Chem. Phys.* **2013**, *139*, 214107.

(83) Landry, B. R.; Falk, M. J.; Subotnik, J. E. Communication: The Correct Interpretation of Surface Hopping Trajectories: How to Calculate Electronic Properties. *J. Chem. Phys.* **2013**, *139*, 211101.

(84) Xu, J.; Wang, L. Branching Corrected Surface Hopping: Resetting Wavefunction Coefficients Based on Judgement of Wave Packet Reflection. *J. Chem. Phys.* **2019**, *150*, 164101.

(85) Shao, C.; Xu, J.; Wang, L. Branching and Phase Corrected Surface Hopping: A Benchmark of Nonadiabatic Dynamics in Multilevel Systems. *J. Chem. Phys.* **2021**, *154*, 234109.

(86) Li, G.; Shao, C.; Xu, J.; Wang, L. A Unified Framework of Mixed Quantum-Classical Dynamics with Trajectory Branching. *J. Chem. Phys.* **2022**, *157*, 214102.

(87) Guo, X.; Xu, J.; Li, G.; Wang, L. Interpretation of Adiabatic and Diabatic Populations from Trajectories of Branching Corrected Surface Hopping. *Chinese J. Chem. Phys.* **2022**, *35*, 488–498.

(88) Subotnik, J. E. Fewest-Switches Surface Hopping and Decoherence in Multiple Dimensions. *J. Phys. Chem. A* **2011**, *115*, 12083–12096.

(89) Shenvi, N.; Subotnik, J. E.; Yang, W. Phase-Corrected Surface Hopping: Correcting the Phase Evolution of the Electronic Wavefunction. *J. Chem. Phys.* **2011**, *135*, 024101.

(90) Bondarenko, A. S.; Tempelaar, R. Overcoming Positivity Violations for Density Matrices in Surface Hopping. *J. Chem. Phys.* **2023**, *158*, 054117.

(91) Colbert, D. T.; Miller, W. H. A Novel Discrete Variable Representation for Quantum Mechanical Reactive Scattering via the *S*-Matrix Kohn Method. *J. Chem. Phys.* **1992**, *96*, 1982–1991.

(92) Manolopoulos, D. E. Derivation and Reflection Properties of a Transmission-Free Absorbing Potential. *J. Chem. Phys.* **2002**, *117*, 9552–9559.

(93) Gonzalez-Lezana, T.; Rackham, E. J.; Manolopoulos, D. E. Quantum Reactive Scattering with a Transmission-Free Absorbing Potential. *J. Chem. Phys.* **2004**, *120*, 2247–2254.

(94) Subotnik, J. E.; Shenvi, N. Decoherence and Surface Hopping: When Can Averaging over Initial Conditions Help Capture the Effects of Wave Packet Separation? *J. Chem. Phys.* **2011**, *134*, 244114.

(95) Tempelaar, R.; van der Vegte, C. P.; Knoester, J.; Jansen, T. L. C. Surface Hopping Modeling of Two-Dimensional Spectra. *J. Chem. Phys.* **2013**, *138*, 164106.

(96) Petit, A. S.; Subotnik, J. E. Calculating Time-Resolved Differential Absorbance Spectra for Ultrafast Pump-Probe Experiments with Surface Hopping Trajectories. *J. Chem. Phys.* **2014**, *141*, 154108.

(97) Petit, A. S.; Subotnik, J. E. How to Calculate Linear Absorption Spectra with

Lifetime Broadening Using Fewest Switches Surface Hopping Trajectories: A Simple Generalization of Ground-State Kubo Theory. *J. Chem. Phys.* **2014**, *141*, 014107.

(98) Petit, A. S.; Subotnik, J. E. Appraisal of Surface Hopping as a Tool for Modeling Condensed Phase Linear Absorption Spectra. *J. Chem. Theory Comput.* **2015**, *11*, 4328–4341.

(99) Li, G.; Shi, Z.; Guo, X.; Wang, L. What is Missing in the Mean Field Description of Spatial Distribution of Population? Important Role of Auxiliary Wave Packets in Trajectory Branching. *J. Phys. Chem. Lett.* **2023**, *14*, 9855–9863.